



Dynamics of palladium single-atoms on graphitic carbon nitride during ethylene hydrogenation



Maurice Vennewald^a, Nina Michelle Sackers^a, Andree Iemhoff^a, Isabella Kappel^b, Claudia Weidenthaler^b, Ansgar Meise^c, Marc Heggen^c, Rafal E. Dunin-Borkowski^c, Luke Keenan^d, Regina Palkovits^{a,e,*}

^aChair of Heterogeneous Catalysis and Chemical Technology, ITMC, RWTH Aachen University, Worringerweg 2, DE-52074 Aachen, Germany

^bMax-Planck-Institut für Kohlenforschung, Kaiser-Wilhelm-Platz 1, DE-45470 Mülheim an der Ruhr, Germany

^cErnst Ruska-Centre for Microscopy and Spectroscopy with Electrons (ER-C), Forschungszentrum Jülich GmbH, DE-52428 Jülich, Germany

^dDiamond Light Source, Harwell Science and Innovation Campus, Didcot OX110DE, United Kingdom

^eMax-Planck-Institute for Chemical Energy Conversion, Stiftstraße 34-36, DE-45470 Mülheim an der Ruhr, Germany

ARTICLE INFO

Article history:

Received 30 November 2022

Revised 24 February 2023

Accepted 3 March 2023

Available online 8 March 2023

Keywords:

Single-atom catalysis
Ethylene hydrogenation
Graphitic carbon nitride
Hydrogenation
Palladium single-atom
H₂-D₂ exchange

ABSTRACT

Single-atoms on carbon–nitrogen supports are considered catalysts for a multitude of reactions. However, doubts remain whether really these species or subnanometer clusters formed under reaction conditions are the active species. In this work, we investigate the dynamics of palladium single-atoms on graphitic carbon nitride during ethylene hydrogenation and H₂-D₂ exchange. By employing aberration-corrected scanning transmission electron microscopy, x-ray photoelectron spectroscopy and x-ray absorption spectroscopy, we will show that palladium, originally present as single-atoms, agglomerates to clusters at 100 °C in a gas atmosphere that contains both ethylene and hydrogen. This agglomeration goes in hand with the emergence of catalytic activity in both ethylene hydrogenation and H₂-D₂ exchange, suggesting that clusters, rather than single-atoms, are the active species. The results presented herein highlight the potential of analytics over the course of reaction to identify the active species and provide new insights into the influence of gas atmosphere on metal speciation.

© 2023 Elsevier Inc. All rights reserved.

1. Introduction

Single-atom heterogeneous catalysts (SAHCs) have gained huge attention in recent years due to maximum metal utilization and unique reactivity [1–4]. Studying their dynamics over the course of reaction has delivered mechanistic insights on the molecular level and helped to unravel the catalytically active species [5–11]. However, most of these studies focus on oxide supports even though carbons – particularly nitrogen containing ones – are frequently employed as support materials for SAHCs [12,13].

Graphitic carbon nitride (g-CN) is one of the most commonly used supports for single-atoms in the class of carbon materials. Due to the semiconductor properties and favorable band gap position of g-CN, SAHCs based on this material are frequently employed in photo- and electrocatalytic applications [14–20]. But also alkyne semi-hydrogenation in liquid [21–23] and gas [24] phase as well as Suzuki coupling [25,26] and oxidation reactions [27,28] were conducted with these types of catalysts.

Lately, some progress has been made in uncovering structure-performance relationships for single-atoms on g-CN. It was shown that the electronic density of the metal center could be influenced by the composition of the support. Higher electron density corresponds with lower stabilization of the single-atom and higher catalytic activity in hydrogenation reactions [23,29]. Furthermore, palladium ensembles consisting of at least three Pd atoms drastically increase activity in alkyne hydrogenation in comparison to single-atoms while diminishing activity in Suzuki coupling [26]. This raises the question of whether single-atoms are actually the active species in hydrogenation reactions or whether clusters form under reaction conditions to drive activity.

Closely related to this question is the question of the bonding environment of the metal, which may include other metal atoms. For Pt single-atoms on g-CN, a recent study delivered new insights. The metal center is coordinated to two pyridine nitrogen functions of the support and two Cl ligands after impregnation and mild temperature treatment at 300 °C (utilizing H₂PtCl₆ as precursor). During treatment at 500 °C, the Cl ligands were removed along with H⁺ from adjacent amine groups from the support. As a result, a Pt complex coordinated to two pyridinic nitrogens and two

* Corresponding author.

E-mail address: palkovits@itmc.rwth-aachen.de (R. Palkovits).

negatively charged amino groups as well as some Pt clusters were formed [30].

This study comes very close to the ultimate goal of fully elucidating the structure of the metal site. However, this structure and especially its evolution under reaction conditions (including agglomeration paths to small metal clusters) remain unclear for most SAHCs. But gaining comprehensive structural understanding is key to establish rational synthesis and treatment procedures for SAHCs [31].

Towards filling this knowledge gap for carbon–nitrogen carriers, and to identify the active species in hydrogenation reactions, we decided to investigate the dynamics of palladium single-atoms on g-CN during ethylene hydrogenation. We chose ethylene hydrogenation as a model reaction because it covers the highly important area of C–C double bond hydrogenation in gas phase. It also allows comparison with the extensive literature on the dynamics of single atoms on oxide supports investigated for this reaction.

For studying the dynamics, we synthesized a palladium single-atom catalyst on exfoliated g-CN (ECN) by impregnation with Pd(NH₃)₄(NO₃)₂ (ECN-Pd-SA) as well as a palladium nanoparticle catalyst (ECN-Pd-NP). We studied their respective catalytic activity in ethylene hydrogenation as well as H₂-D₂ exchange and concluded that a Pd(N_{ECN})₂(NO₃) complex that is formed after impregnation agglomerates at 100 °C in an atmosphere that consists of both ethylene and hydrogen to form clusters that are the active species for both types of reaction.

2. Experimental

2.1. Material synthesis

The support was synthesized by treating melamine (20 g) in a CWF 1100 muffle furnace (Carbolite) for 4 h at 550 °C (2.3 °C min⁻¹). The resulting bulk graphitic carbon nitride (BCN) was pulverized. Exfoliated graphitic carbon nitride (ECN) was synthesized by grinding BCN (1.7 g) in a ball mill (Pulverisette 23, Fritsch) (50 Hz, 5 min) and then treating it in a muffle furnace (porcelain bowl, 50 mg cm⁻²) for 4 h at 500 °C (2.3 °C min⁻¹).

ECN-Pd-SA was synthesized by adding Pd(NH₃)₄(NO₃)₂ – 10 wt % solution (421 µL, 0.5 wt% Pd relative to the support) to water (500 mL). Then ECN (3 g, 6 mg mL⁻¹-solution) was added, stirred for 4 h and then filtered and washed with water (300 mL). The resulting solid was dried in high vacuum and stored under argon.

ECN-Pd-NP was synthesized by dissolving K₂PdCl₄ (30.7 mg, 0.5 wt% Pd relative to the support) in aqueous HCl (0.5 mM, 333 mL). Then aqueous NaBH₄ (1.9 mL, 0.1 M) followed by ECN (2 g, 6 mg mL⁻¹-solution) were added and stirred for 4 h. The material was filtered and washed with water (300 mL) and then dried at 80 °C.

2.2. Analytical methods

Elemental analysis (CHN) was carried out by Mikrolab Kolbe, Oberhausen.

Optical emission spectrometry with inductively coupled plasma (ICP-OES) for the determination of the metal content was carried out by Mikrolab Kolbe, Oberhausen.

Nitrogen physisorption isotherms were recorded at 77 K using a Quadrasorb SI instrument. Before measurement, the samples were degassed for at least 5 h at 150 °C with a FloVac degasser under vacuum (0.35 mbar). The data were evaluated using the QuadraWin software package. The specific surfaces were determined according to the BET model in the range 0.05 ≤ p/p₀ ≤ 0.25.

Infrared spectra were recorded using a Vertex70 spectrometer (Bruker) equipped with a Praying Mantis High Temperature Reaction Chamber (Harrick Scientific Products) in DRIFTS mode. Before each measurement, the sample was baked in nitrogen (50 mL min⁻¹) at 50 °C for 1 h and then measured against a KBr background. Then CO (50% CO/He, 30 mL min⁻¹) was flown over the sample for 10 min followed by desorption in nitrogen (50 mL min⁻¹). Evaluation was carried out using the software OPUS 6.5 (Bruker).

X-ray diffraction (XRD) patterns were measured on a Stoe STADI P transmission diffractometer (Debye-Scherrer geometry) using 0.7 mm borosilicate capillaries. The diffractometer was equipped with a primary Ge(111) monochromator (MoKα₁ radiation λ = 0.7093 Å) and a position-sensitive Mythen1K detector. Data were collected in the range of 2θ = 3–120°.

For the experimental verification of Pd single atoms and nano particles, the specimens were investigated applying aberration-corrected scanning transmission electron microscopy (AC-STEM). The ECN-supported Pd-substrate was suspended in EtOH and prepared on a holey carbon Cu TEM grid via drop-cast method. The suspension was evaporated in air. Subsequently, the specimens were cleaned by a UV-based sample cleaner (Hitachi HT ZONETEM II). High-resolution imaging was conducted on a Hitachi HF5000 and a FEI TITAN ChemiSTEM, both, operating at 200 kV and equipped with a spherical-aberration (Cs) probe corrector.

X-ray photoelectron spectroscopy (XPS) measurements were performed with a SPECS GmbH spectrometer equipped with a PHOIBOS 150 1D-DLD hemispherical energy analyzer. The monochromatized Al Kα X-ray source (E = 1486.6 eV) was operated at 15 kV and 200 W. For the narrow scans, a pass energy of 20 eV was applied. The medium area mode was used as the lens mode. The base pressure during the experiment in the analysis chamber was 5 × 10⁻¹⁰ mbar. To account for charging effects, all spectra were referred to the C–C/C–H contribution of the C1s signal (284.5 eV). The program CasaXPS Version 2.3.22PR1.0 was used for data evaluation.

An asymmetric peak shape function LA(1.9,7,2) was used for the fitting of the metallic Pd species. For the Pd species with different oxidation states symmetric profile functions, GL(30), were used for fitting. The average peak position (P_a) was calculated by summing the arithmetic products of the peak positions with their respective relative contributions for the different contributions according to equation (1):

$$P_a = P_i A_i + P_{ii} A_{ii} \quad (1)$$

P_x: peak position of component x; A_x: relative peak intensity of component x.

For the fitting of the sp³ carbon in the C1s spectrum the asymmetric peak shape function LA(2,3,0) was applied. A symmetric peak shape function GL(30) was used to fit the Carbon in the Triazine rings while the satellite features were fitted using LA(1.3, 2.43).

The O1s spectrum was fitted using the symmetric peak shape function GL(30).

The symmetric peak shape function GL(30) was applied for the fitting of the three main species in the N1s spectrum. The satellite features were fitted using LA(1.3, 2.43).

The assignment of signals was done based on a work by Morgan.[32].

X-ray absorption spectroscopy at the Pd K edge (24350 eV) was performed at the Diamond Light Source beamline I20-EDE.[33,34]. A bent Si (311) crystal was used to focus the polychromatic beam on the sample. Data was collected in transmission mode using the position dependent XH detector with an energy resolution of 0.5 eV.[35] Samples were either prepared as pellets (1.2 g) for

ex-situ experiments or pelletized and sieved (125–200 μm) for in-situ experiments. For in-situ experiments the samples with a Pd content of 0.77 wt% were filled into a quartz tube with an inner diameter of 5.5 mm. An identical tube filled with BN (88–177 μm) was used as background. Samples were first pretreated for 2 h in Ar (40 mL min^{-1}) at 50 $^{\circ}\text{C}$. Then the gas flow was switched to a 2 % H_2 /2 % ethylene/Ar mixture. Then a temperature program with 2 h at 50, 100 and 150 $^{\circ}\text{C}$ as well as 4 h at 200 $^{\circ}\text{C}$ (10 $^{\circ}\text{C min}^{-1}$) was conducted. Spectra were taken at the beginning and at the end of each temperature step as well as after 1.

The resulting spectra were background corrected and normalized at the height of the edge step using the Athena program from the Demeter software package. EXAFS fits were conducted employing the Artemis program.[36] The edge position was defined as the first minimum of the first derivative. The pre-edge range was set to –200 to –150 eV relative to the edge position and the normalization range to 150 to 1140 eV. Forward fourier transform (FFT) was performed in k space from 3 to 8 \AA^{-1} for in-situ samples, 3 to 10 \AA^{-1} for ex-situ samples and 3 to 12 \AA^{-1} for references in accordance with the respective data quality.

2.3. Catalytic studies

Reaction rates were measured in a gas phase reactor (made by the institute). The gas flows were controlled with mass flow controllers (Bronkhorst/MKS Instruments). For ethylene hydrogenation, the concentrations of H_2 (amu 2), ethylene (amu 28) and ethane (amu 31) were measured using a Cirrus 2 mass spectrometer (MKS Instruments) with He as internal reference. For the H_2 - D_2 exchange reaction, the signals of H_2 (amu 2), HD (amu 3) and D_2 (amu 4) were measured without internal reference.

Samples were held on a porous quartz disc (4.2 mm diameter) covered with 1 mm quartz wool in a U-shaped quartz reactor. The temperature was measured inside the catalyst bed with a temperature sensor.

For ethylene hydrogenation experiments, diluted samples (99:1; dilutant: ECN) were heated in a 10 % He/Ar gas stream (100 mL min^{-1}) to 50 $^{\circ}\text{C}$ at 10 $^{\circ}\text{C min}^{-1}$ and held for 2 h before reaction. Then the gas flow was switched to bypass and adjusted to 2 % H_2 / 2 % ethylene/ 10 % He/ Ar (100 mL min^{-1} ; GHSV = 90000 h^{-1}). After stabilization, the flow was switched to the reactor. The point in time 1 min after this switching process was defined as $t = 0$. In a typical experiment, the temperature was kept at 50, 100 and 150 $^{\circ}\text{C}$ for 2 h each and at 200 $^{\circ}\text{C}$ for 14 h (10 $^{\circ}\text{C min}^{-1}$). Turnover and yield were calculated as the difference between bypass concentration (5 min average) and reactor concentration for each data point (measured every 3 s). Conversion is presented as a moving average of 200 data points.

For H_2 - D_2 exchange experiments, diluted samples (99:1; dilutant: ECN) were heated in a 10 % He/Ar gas stream (100 mL min^{-1}) to 50 $^{\circ}\text{C}$ at 10 $^{\circ}\text{C min}^{-1}$ and held for 2 h before reaction. Then the gas flow was switched to bypass and adjusted to 2 % H_2 / 2 % D_2 / 10 % He/ Ar (100 mL min^{-1} ; GHSV = 90000 h^{-1}). After stabilization, the flow was switched to the reactor. The point in time 1 min after this switching process was defined as $t = 0$. In a typical experiment, the temperature was kept at 50, 100, 150 and 200 $^{\circ}\text{C}$ for 2 h each (10 $^{\circ}\text{C min}^{-1}$). The signal for HD was normalized for each data point (measurement every 3 s) with the bypass signal (5 min average). This normalized HD signal is presented as a moving average of 200 data points.

2.4. Computational details

Periodic density functional theory calculations were performed using the VASP program series (revision 5.4.4)[37,38] in combination with the PBE exchange–correlation functional[39] within the

framework of the generalized-gradient approximation (GGA). The dDsC correction was used to account for dispersion.[40] The electron–ion interactions were described by the PAW method.[41,42] The energy cut-off of the plane wave basis was set to 600 eV to ensure accurate energies. The ideal g–CN was modeled in AB stacking of two corrugated g–CN layers in a hexagonal cell ($a = b = 6.97 \text{ \AA}$, $c = 6.66 \text{ \AA}$). The investigated slab consisted of a two-layered (2×2) supercell with a 10 \AA vacuum overlayer to avoid interactions between the slabs. Defective g–CN was studied in the same supercell. The Brillouin-zone was sampled by a Γ -centered $3 \times 3 \times 1$ Monkhorst-Pack grid [43] together with a Gaussian smearing of 0.05 eV. The geometry optimizations of local minima were carried out with convergence criteria for the electronic self-consistent energy and the ionic relaxation of 10^{-6} eV and 0.02 eV \AA^{-1} , respectively. Zero-point energy and thermal contributions to the electronic energy were determined from frequency calculations of the free molecules as well as the metal and ligands interacting with the g–CN support using statistical thermodynamics at a temperature of 20 $^{\circ}\text{C}$ and atmospheric pressure [44]. For the metal species adsorbed to the g–CN framework, the harmonic limit was applied for the calculation of thermal contributions. In all cases, low-frequency modes below 100 cm^{-1} were shifted to 100 cm^{-1} for the calculation of the vibrational entropy and enthalpy. Formation energies ΔG_{form} were calculated using Eq. (2), where G denotes the Gibbs energies of the Pd precursor complex (prec), the ideal or defective g–CN (g–CN), the Pd immobilized on g–CN (Pd/g–CN) and the free ligands from the Pd precursor (lig).

$$\Delta G_{\text{ads}} = G_{\text{Pd/g-CN}} + G_{\text{lig}} - (G_{\text{g-CN}} + G_{\text{prec}}) \quad (2)$$

Initial-state calculations were performed to obtain the core-level shifts with reference to a Pd surface atom of a Pd(111) slab.

3. Results and first discussion

3.1. Synthesis of ECN-Pd-SA and ECN-Pd-NP

Exfoliated graphitic carbon nitride (ECN) was synthesized according to the procedure reported by Chen *et al.* with the modification of using melamine instead of dicyandiamide as the starting substrate [22]. Analytical results (N_2 -physisorption, elemental analysis, XRD, IR and XPS) can be found in the SI, are practically identical to the results obtained by Chen *et al.* and confirm the successful synthesis of ECN (Table S 1, Fig. S 1–6). With an elemental formula of $\text{C}_3\text{H}_{2.22}\text{N}_{4.55}\text{O}_{0.26}$, there is a notable difference to the idealized formula of C_3N_4 . This opens the possibility of alternative coordination sites for Pd, including N- H_x and oxygen functionalities, the presence of which is confirmed by XPS and IR data (Fig. S 2, S 5 and S 6).

Impregnation of ECN with $\text{Pd}(\text{NH}_3)_4(\text{NO}_3)_2$ and palladium nanoparticles yields materials with palladium contents close to the targeted 0.5 wt% (Table S 1). Analyses via aberration corrected STEM, XPS and XAS were conducted to investigate the metal speciation. AC-STEM reveals the presence of single-atoms for ECN-Pd-SA (Fig. 1 a/b) and nanoparticles for ECN-Pd-NP (Fig. 1 c/d). Further images confirming these results can be found in the SI (Fig. S 11 and S 12). Note however that we cannot fully exclude the presence of sub-nanometer clusters for ECN-Pd-SA. Movement of the palladium under the electron beam, the relatively low contrast and the lack of resolution in z-direction make distinguishing single-atoms and subnanometer clusters ambiguous. A clear picture therefore only emerges if all analytical methods are considered together. XPS shows two Pd $3d_{5/2}$ contributions for both samples at 335.1 and 337.6 eV (NP) and at 336.4 and 338.1 eV (SA) (Fig. 1 e). The values for ECN-Pd-NP fit to a mixture of Pd^0 (dominant) and Pd^{2+} , consistent with partly oxidized nanoparticles. The values

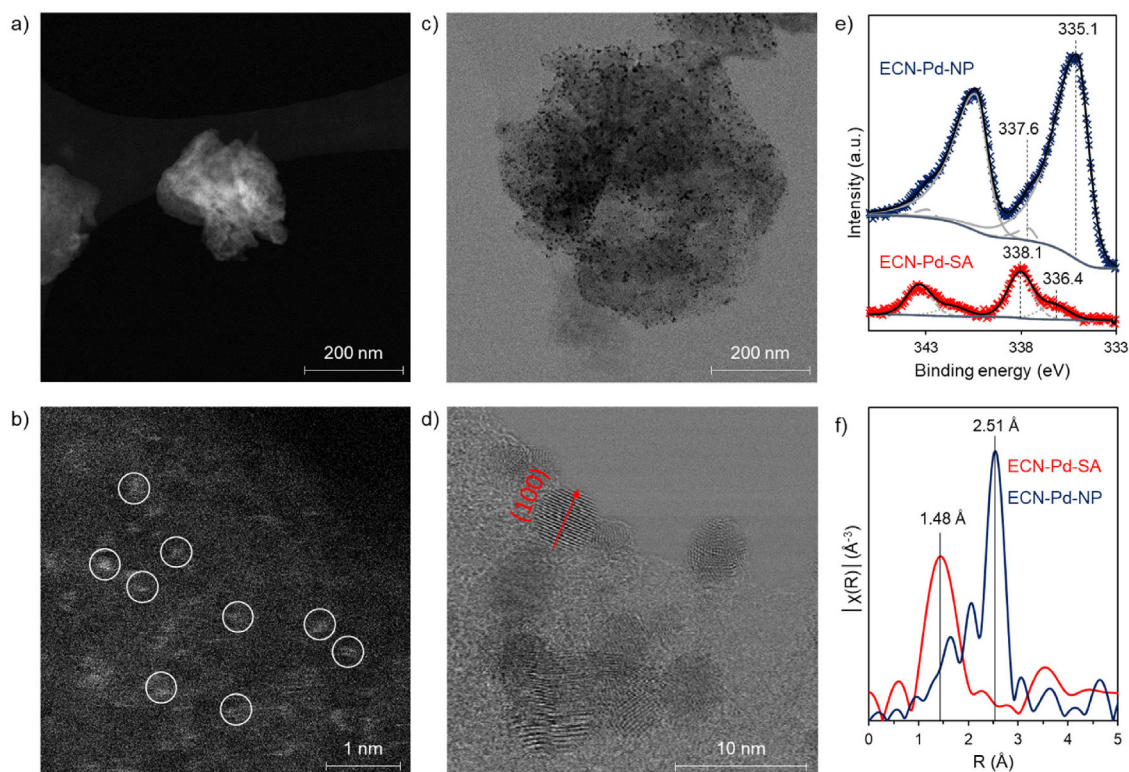


Fig. 1. (a,b) Dark field AC-STEM images of ECN-Pd-SA. As a guide to the eye, some single-atoms are marked with white circles. (c,d) Bright field AC-STEM images of ECN-Pd-NP. (e) Pd 3d core level XPS spectra of ECN-Pd-NP (blue) and ECN-Pd-SA (red). With black lines showing fits to the raw data (crosses) and grey lines deconvolution into components. Positions of Pd 3d 5/2 components are shown by vertical lines. (f) Normalized magnitudes of the k^2 -weighted Fourier transform (FT) of the extended X-ray absorption fine structure spectra in radial distance (not phase corrected). (For interpretation of the references to color in this figure legend, the reader is referred to the web version of this article.)

for ECN-Pd-SA lie in the range of different Pd^{2+} references (336.3 eV for PdO [45] and 338.4 eV for PdCl_2 [46]) and will be discussed in more detail in section 3.1. XAS reveals edge positions consistent with Pd^0 (ECN-Pd-NP) and Pd^{2+} (ECN-Pd-SA) (Fig. S 7). Not phase-corrected Fourier transform yields main peaks at 1.48 Å (ECN-Pd-SA) and 2.51 Å (ECN-Pd-NP), consistent with Pd-N/O and Pd-Pd interactions, respectively (Fig. 1 f). In particular, no signs for Pd-Pd interactions are found for ECN-Pd-SA. Overall, comprehensive analyses indicate the presence of single-atoms for ECN-Pd-SA and of nanoparticles for ECN-Pd-NP. The designations ECN-Pd-SA and ECN-Pd-NP are therefore rightly attributed to these two materials.

3.2. Comparison of the catalytic activity of ECN-Pd-SA and ECN-Pd-NP

To investigate the interrelationships between the properties of the metal, catalytic activity and reaction conditions, ECN-Pd-SA as well as ECN-Pd-NP were subjected to a temperature treatment in ethylene hydrogenation consisting of subsequent periods of 2 h at 50 °C, 100 °C and 150 °C and at least 14 h at 200 °C after pre-treatment in argon. During this treatment, highly differing profiles in ethylene conversion of ECN-Pd-SA and ECN-Pd-NP become apparent (Fig. 2 a). While ECN-Pd-NP shows instantaneous activity at 50 °C and a further rapid increase of ethylene conversion over the course of 2 h, the single-atom catalyst is inactive at 50 °C for the entire 2 h. This changes when the temperature increases to 100 °C. At this temperature, ethylene conversion rises from 0 % to 16 % over 2 h time on stream (TOS). This activation continues when switching to 150 °C, but at a much slower rate (from 16 % to 18 % in 2 h). At 200 °C, a sudden decrease in conversion occurs, followed by slow activation (4 to 18 % conversion in 14 h).

ECN-Pd-NP also shows activation during all temperature steps. However, activity rises faster with increasing temperature. Another significant difference in comparison to ECN-Pd-SA is the decrease in activity when the temperature rises from 100 to 150 °C, while it remains constant for the single-atom catalyst.

To investigate the general ability of the two materials to activate hydrogen, H_2 - D_2 exchange reactions were carried out using the same procedure as for ethylene hydrogenation. In this case, the differences between the two catalysts are even more pronounced (Fig. 2 b). The normalized HD signal - defined as the HD signal measured in the output stream divided by the HD signal measured in the bypass - remains constant at about 1 for ECN-Pd-SA over the entire period. This leads to the conclusion that no H_2 - D_2 exchange is catalyzed by ECN-Pd-SA and, in contrast to ethylene hydrogenation, no activation takes place during the reaction.

In contrast, the NP catalyst already showed a normalized HD signal of 4.2 at the start, which increases to 4.8 within 20 min and then remains constant. A change of the temperature to 100 °C leads to an increase to 5.0 - close to the equilibrium value of 5.1 - and a subsequent drop to 4.9 over 2 h TOS. Increasing the temperature to 150 °C causes the signal to rise again to 5.0 for a short time, only to drop to 4.9 in the following 2 h. A further increase of the temperature to 200 °C results in a decrease to 4.7 with a further decline to 4.6 over 2 h.

This behavior in H_2 - D_2 exchange is markedly different from ethylene hydrogenation as ECN-Pd-NP deactivates over the course of the reaction, whereas activation is observed for the latter reaction. Together with the lack of activation of ECN-Pd-SA, this result shows the crucial role that ethylene plays in the activation process.

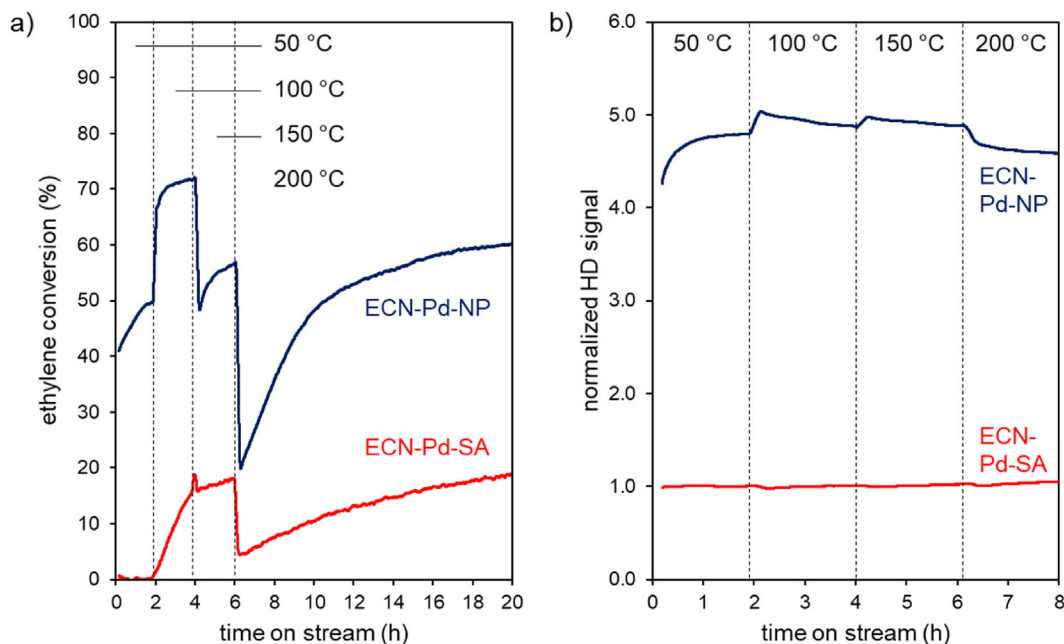


Fig. 2. (a) Ethylene conversion with ECN-Pd-SA (red, lower line) and ECN-Pd-NP (blue, upper line) in ethylene hydrogenation (2 % ethylene/2 % hydrogen/20 % helium/76 % argon; 100 mL min^{-1} GHSV = 90000 h^{-1}). (b) Normalized HD signal in HD exchange reaction (2 % deuterium/2 % hydrogen/96 % argon; 100 mL min^{-1} GHSV = 90000 h^{-1}). Reaction temperature is indicated by vertical lines. Pretreatment: 20 % helium/80 % argon; 100 mL min^{-1} GHSV = 90000 h^{-1} ; $T = 50 \text{ }^\circ\text{C}$). (For interpretation of the references to color in this figure legend, the reader is referred to the web version of this article.)

3.3. Evolution of ECN-Pd-SA during ethylene hydrogenation

ECN-Pd-SA transformed from a catalytically inactive to an active material in ethylene hydrogenation at $100 \text{ }^\circ\text{C}$. In order to correlate this activation with metal speciation and electronic properties of Pd over the course of reaction, AC-STEM, XPS and XAS measurements of the as-made sample (ECN-Pd-SA), after 2 h at $50 \text{ }^\circ\text{C}$ in ethylene hydrogenation (ECN-Pd-SA- $50 \text{ }^\circ\text{C}$), after further 2 h at $100 \text{ }^\circ\text{C}$ (ECN-Pd-SA- $100 \text{ }^\circ\text{C}$) and after another 2 h at $150 \text{ }^\circ\text{C}$ plus 42 h at $200 \text{ }^\circ\text{C}$ (ECN-Pd-SA- $200 \text{ }^\circ\text{C}$) were conducted (Fig. S 10).

As discussed in section 2.1, AC-STEM emphasizes the presence of isolated metal species after impregnation. Isolated metal species remain dominant in the other samples (Fig. 3). The term isolated metal species refers herein to single-atoms as well as subnanometer clusters due to the difficulties in distinguishing between these two that were discussed in section 2.1. In addition to the possible presence of clusters, nanoparticles of varying size are identified in ECN-Pd-SA- $50 \text{ }^\circ\text{C}$, ECN-Pd-SA- $100 \text{ }^\circ\text{C}$ and ECN-Pd-SA- $200 \text{ }^\circ\text{C}$ (Fig. S 13). Due to their very irregular and low frequency of occurrence, no statistically significant statement on the presence of nanoparticles can be drawn from our AC-STEM dataset.

XPS results for ECN-Pd-SA show two $\text{Pd}3d_{5/2}$ photopeaks at 336.4 and 338.1 eV with relative areas of 26 and 74 %. This is in the range of Pd^{2+} species (336.3 eV for PdO [45] and 338.4 eV for PdCl_2 [46]) but clearly indicates the presence of at least two distinct palladium species with different electron densities. The average value (the sum of the peak positions weighted by their relative intensities) is 337.6 eV. Although the peak positions and relative intensities differ slightly for ECN-Pd-SA- $50 \text{ }^\circ\text{C}$, this average value remains constant. For ECN-Pd-SA- $100 \text{ }^\circ\text{C}$ the average value decreases only slightly to 337.5 eV (Fig. 4, Table S 3). In contrast, a significant change in relative peak intensities and peak positions is visible for ECN-Pd-SA- $200 \text{ }^\circ\text{C}$. The photopeak at 336.0 eV contributes about 36 % of the total $\text{Pd}3d_{5/2}$ peak area, whereas the higher energy contribution at 337.8 eV shrinks to 64 %. This results in an average value of 337.2 eV.

The XPS results indicate that no huge differences in terms of Pd electron density exist between ECN-Pd-SA, ECN-Pd-SA- $50 \text{ }^\circ\text{C}$ and ECN-Pd-SA- $100 \text{ }^\circ\text{C}$ suggesting that the nanoparticles observed in STEM for the latter two samples represent only a small fraction of the total palladium species. Interestingly, there is also only a very small difference between ECN-Pd-SA and ECN-Pd-SA- $50 \text{ }^\circ\text{C}$ on the one hand and ECN-Pd-SA- $100 \text{ }^\circ\text{C}$ on the other, although, significant changes in catalytic activity are observed (Fig. 1 a). This finding might be explained in two ways: (1) the change in catalytic activity is not accompanied by a change in electron density or (2) catalytic activity is driven by a very active species that is present in minor amounts and therefore hardly detectable by XPS. In general, it should be noted that the metal amounts employed here are close to the detection limits for lab-based XPS analytics.

The significant change in the average value for ECN-Pd-SA- $200 \text{ }^\circ\text{C}$ compared to the previous samples is attributed to the formation of significant amounts of Pd nanoparticles. A Pd^0 contribution is usually expected at around 335.1 eV (Pd foil) but is shifted to higher values if the particles are small [47] (as can be inferred from STEM) and have a strong interaction with an electron withdrawing support [48]. In general, XPS alone is not sufficient to differentiate between a change in ligand environment and redox processes and consequently requires complementary methods to investigate the chemical environment around the metal center.

Compared to laboratory-based XPS, synchrotron-based XAS offers a lower detection limit while penetrating a larger portion of the sample [49]. Consequently, employing XAS made it possible to obtain more information about the chemical environment and electronic state of palladium. Measurements yield edge positions (first minimum of the first derivative) for all materials consistent with an oxidation state of +2. However, subtle differences between the materials emerge. While the edge position remains practically unchanged between ECN-Pd-SA and ECN-Pd-SA- $50 \text{ }^\circ\text{C}$, it moves to slightly lower values for ECN-Pd-SA- $100 \text{ }^\circ\text{C}$ and further for ECN-Pd-SA- $200 \text{ }^\circ\text{C}$ (Fig. 5 a). Still, it does not reach the value of Pd^0 . Furthermore, a decrease in white line intensity occurs over the course of reaction. The differences between the respective samples follow

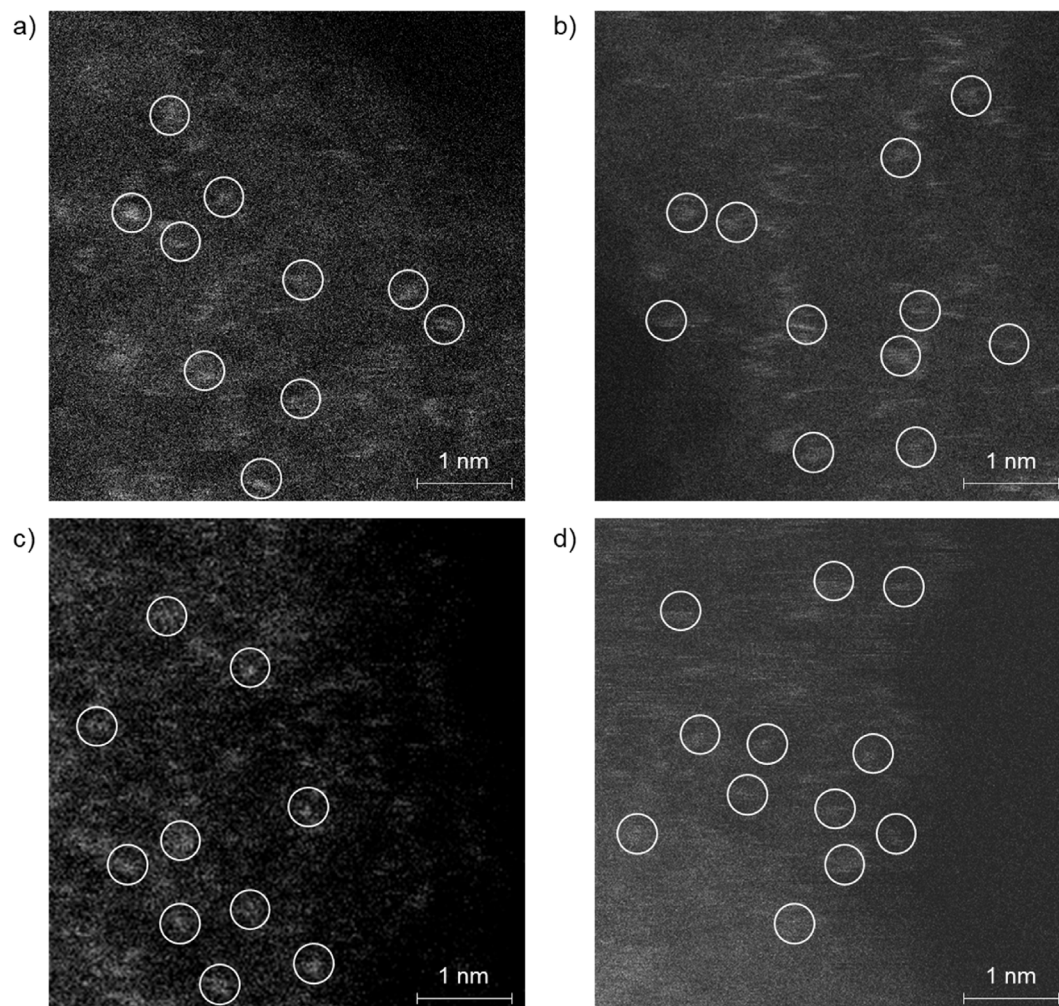


Fig. 3. AC-STEM images of (a) ECN-Pd-SA, (b) ECN-Pd-SA-50 °C, (c) ECN-Pd-SA-100 °C and (d) ECN-Pd-SA-200 °C. As a guide to the eye, some single-atoms are marked with white circles.

the same trend as for the edge position. These results suggest that the emergence of catalytic activity is linked to an increase in electron density for palladium.

Not phase-corrected Fourier transformation of the EXAFS of ECN-Pd-SA shows a main peak at 1.48 Å in R space, corresponding to a Pd-N or Pd-O interaction (see references in Fig. S 8). No significant other contribution is identified. Especially no Pd-Pd interaction at 2.51 Å is detected. Comparing ECN-Pd-SA with ECN-Pd-SA-50 °C reveals no differences apart from a small decrease in the main peak. This indicates that the metal retains a single-atom nature at this temperature, which is associated with inactivity in ethylene hydrogenation.

However, consistent with activation at 100 °C, significant changes in the EXAFS spectrum of ECN-Pd-SA-100 °C are detectable: the main peak intensity decreases, while at the same time a peak at about 2.51 Å gains in intensity. For ECN-Pd-SA-200 °C, this trend continues and a peak with a maximum at 2.46 Å becomes apparent. We attribute this peak to Pd-Pd interactions in accordance with the STEM results that show formation of nanoparticles and XPS results suggesting on average a more electron rich Pd. The lower value of this peak compared to Pd-foil (2.51 Å) can be explained by smaller domain size of the nanoparticles resulting in smaller Pd-Pd bond distances [50]. We judge the increase in intensity for the same peak in the ECN-Pd-SA-100 °C as significant considering the quasi identity of the ECN-Pd-SA and ECN-Pd-SA-

50 °C samples. In addition, these results are underlined by *in-operando* XAS on a sample with 0.77 wt% Pd loading (Fig. S 17). We therefore ascribe arising catalytic activity of ECN-Pd-SA in ethylene hydrogenation at 100 °C to the formation of Pd clusters and (small) nanoparticles.

3.4. Investigation of the role of gas atmosphere in the activation of ECN-Pd-SA

To gain further insights into the role of gas atmosphere in the activation process of ECN-Pd-SA, ethylene hydrogenation and H₂-D₂ exchange experiments according to the procedure described above were conducted after a pretreatment in different atmospheres. For this, the regular pretreatment in argon and then the first two temperature steps (2 h at 50 °C, 2 h at 100 °C) of the known procedure were conducted with 2 % hydrogen, 2 % ethylene or 2 % ethylene/hydrogen (Scheme S 1). The aim is to investigate whether only one of the two gases can lead to the same activation as observed for ethylene hydrogenation. In addition, the effect of prior activation of the catalyst during ethylene hydrogenation at 100 °C on the activity during a re-run of the temperature program is investigated.

After conducting ethylene hydrogenation as pretreatment, significant and stable conversion (2 %) in ethylene hydrogenation even at 50 °C is visible (Fig. 6 a). After switching to 100 °C, the

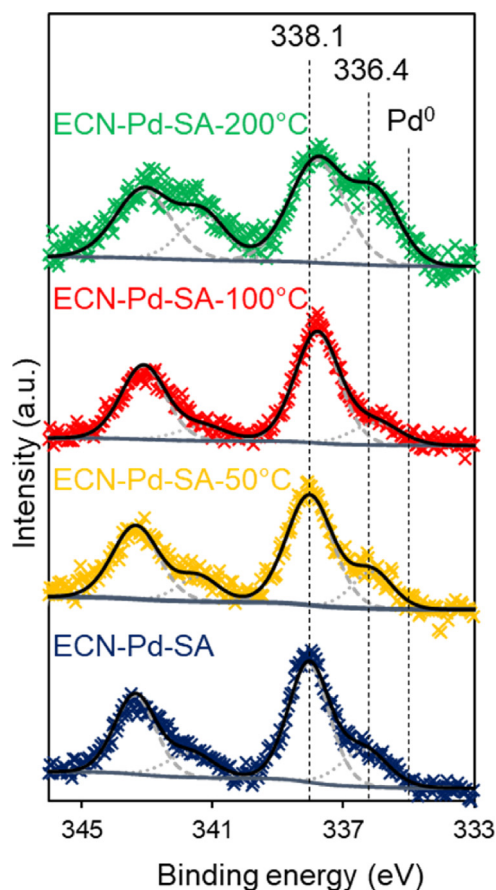


Fig. 4. Normalized Pd 3d core level XPS spectra of ECN-Pd-SA over the course of reaction. Black lines show fits to the raw data (crosses), grey lines deconvolution into components and blue lines the background. (For interpretation of the references to color in this figure legend, the reader is referred to the web version of this article.)

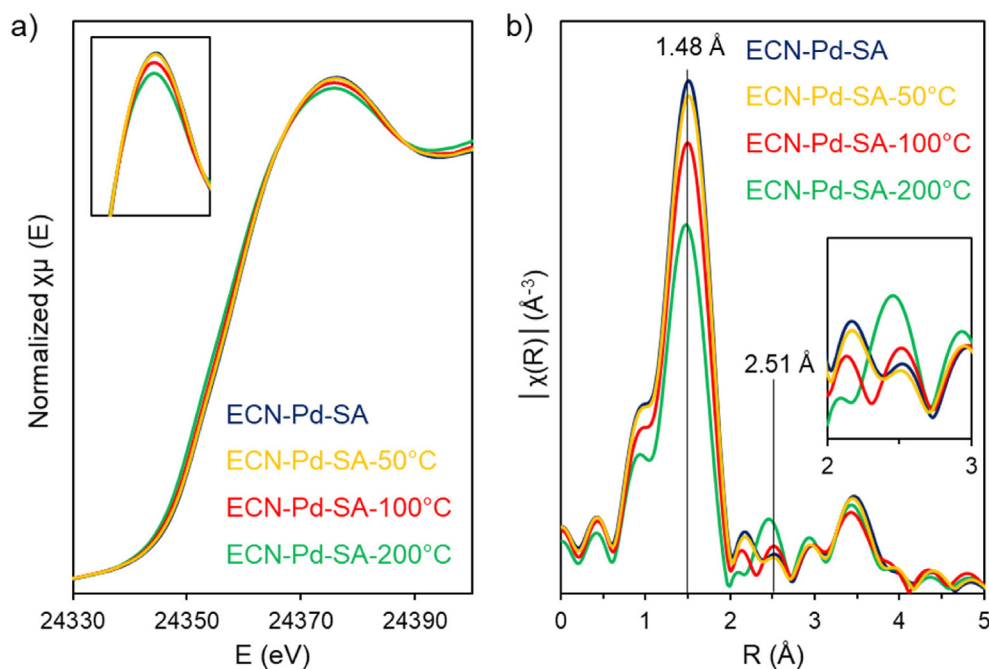


Fig. 5. (a) XANES spectra of ECN-Pd-SA samples over the course of reaction. Inset: Zoom into the 24,360 to 24,390 eV region (a). (b) Normalized magnitudes of the k^2 -weighted Fourier transform (FT) of the extended X-ray absorption fine structure spectra in radial distance (not phase corrected) of the same samples. Inset: Zoom into the 2 to 3 Å region (b).

conversion abruptly increases to 11 % instead of showing the slow activation behavior of the untreated material. In agreement with the behavior of the catalysts without prior ethylene hydrogenation pretreatment, further activation is then observed at 100, 150 and 200 °C. This resembles the behavior of ECN-Pd-NP, further underlining the assumption that clusters/nanoparticles are the active species in ethylene hydrogenation.

A pretreatment in only hydrogen or ethylene at 100 °C results in markedly different results. No conversion is observed at 50 °C after such treatments (Fig. 6 a). This illustrates that a pretreatment in only one of these gases is not able to induce the formation of clusters/nanoparticles. Interestingly, this pretreatment even has a negative effect on activation in ethylene hydrogenation at 100 °C. Whereas ECN-Pd-SA reaches 16 % conversion in ethylene hydrogenation after 2 h at 100 °C without prior treatment, only 5 % and 2 % are reached after treatment in either ethylene or hydrogen. However, this retained activation is reversed at 150 °C where faster activation compared to the case of no pretreatment or pretreatment in ethylene and hydrogen occurs. After 2 further hours at 150 °C the samples pretreated in hydrogen or ethylene reach about 19 % conversion, whereas the untreated sample reaches 18 % and the sample pretreated in ethylene and hydrogen reaches 25 %. This trend continues at 200 °C with the hydrogen pretreated sample allowing highest conversion with 40 % after 20 h TOS.

These results emphasize that pretreatment in hydrogen or ethylene formed metal species that are slower to agglomerate to clusters at 100 °C and therefore can be assumed to be more stable. On the other hand, these species are still prone to agglomeration at higher temperature (150 and 200 °C). Activation at these higher temperatures is therefore faster, as metal species that would have already agglomerated at lower temperature without pretreatment now undergo fast agglomeration together with species that only agglomerate at higher temperatures.

For H_2 - D_2 exchange, the different pretreatments have even greater effects on catalytic activity. The normalized HD signal is between 0.9 and 1.1 at 50, 100 and 150 °C after pretreatment in either only hydrogen or ethylene; essentially revealing an inactive

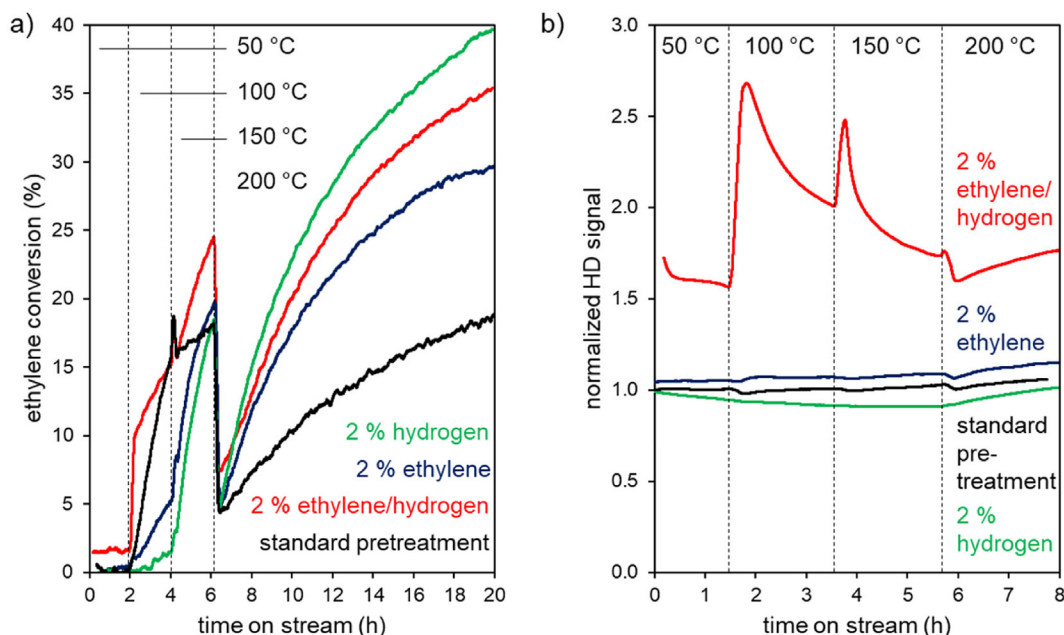


Fig. 6. (a) Ethylene conversion in ethylene hydrogenation (2 % ethylene/2 % hydrogen/ 20 % helium/76 % argon; 100 mL min^{-1} GHSV = 90000 h^{-1}) and (b) normalized HD signal in HD exchange reaction (2 % deuterium/2 % hydrogen/96 % argon; 100 mL min^{-1} GHSV = 90000 h^{-1}) after pretreatment for 2 h at 50 °C in Ar (black) and 2 h at 50 °C and 100 °C in 2 % ethylene/2 % hydrogen/96 % argon (red), 2 % ethylene/98 % argon (blue) or 2 % hydrogen/98 % argon (green). (For interpretation of the references to color in this figure legend, the reader is referred to the web version of this article.)

catalyst within the margin of error. At 200 °C, slow activation in $\text{H}_2\text{-D}_2$ exchange can be inferred.

After conducting ethylene hydrogenation as pretreatment, a different behavior is observed. The normalized HD signal stabilizes around 1.6 at 50 °C after an initially higher value. Raising the temperature to 100 °C causes the signal to jump to 2.7, decreasing to 2.0 over the course of 2 h. A similar process is observed when switching to 150 °C albeit with faster deactivation. When switching to 200 °C the activity first drops and then increases slowly.

These results underline the need for both ethylene AND hydrogen for the activation process. Furthermore, treatment in an atmosphere that only contains hydrogen leads to deactivation instead of activation at lower temperatures (100 and 150 °C), whereas slow activation at 200 °C can occur. In contrast, treatment of the activated catalyst in an ethylene atmosphere has no effect on the activity (Fig. S. 20). This further highlights the complex influence of gas composition and temperature on the agglomeration process.

3.5. DFT calculations

In order to gain insight into the structure of palladium species, we calculated Pd core level binding energies and formation Gibbs energies for different types of binding environments. A Pd^{2+} species coordinating to two L and two X-type ligands in a square-planar geometry was assumed. For the X ligand, we chose NO_3^- which is present in the precursor complex $\text{Pd}(\text{NH}_3)_4(\text{NO}_3)_2$ and OH^- , which might replace NO_3^- in water. As a reference, the core level shift for Cl^- , that might be present when K_2PdCl_4 instead of $\text{Pd}(\text{NH}_3)_4(\text{NO}_3)_2$ is employed as a precursor, is also calculated. For all these calculations, we assumed two pyridinic nitrogen sites of the support as L ligands (Fig. 7 a),b,c); for sideview see Fig. S 19), which are the dominant N species according to XPS.

The shift in core level binding energy relative to a surface Pd in a Pd(111) slab is 5 eV for NO_3^- as X ligand, 4.6 eV in case of Cl^- and 3.6 eV in case of OH^- . This underlines the huge influence of the ligand sphere and consequently the precursor complex on the electronic properties of Pd. Interestingly, the XPS spectrum of ECN that

was impregnated with K_2PdCl_4 is quasi identical to the spectrum obtained from $\text{Pd}(\text{NH}_3)_4(\text{NO}_3)_2$ but shifted 0.35 eV to lower binding energies (Fig. S 18). This is in very good agreement with the presence of Cl^- and NO_3^- , respectively, as X ligands.

Apart from pyridinic nitrogen groups, elemental analysis and XPS also reveal the presence of N-H_x and oxygen functionalities on the support (section 2.1). In order to investigate the influence of such functionalities, we replaced one pyridinic nitrogen in the complex $\text{Pd}(\text{N}_{\text{py}})_2(\text{NO}_3)_2$ with an imine or a carbonyl function (Fig. 7 d) and e)). Core level binding energies lower by 0.4 eV and 0.3 eV, respectively, are found. Furthermore, clear effects on formation energy are observed. Relative to the relaxed scaffold and Pd $(\text{NH}_3)_4(\text{NO}_3)_2$, the formation of c) and e) is endergonic with 9 kJ mol^{-1} and 41 kJ mol^{-1} , while the formation of d) is slightly exergonic with -6 kJ mol^{-1} . This suggests an energetically unfavorable coordination to oxygen compared to nitrogen functionalities and that there is a small energetic advantage for coordination of Pd to N-H_x functionalities compared to pyridinic nitrogen.

4. Discussion

4.1. Structure of ECN-Pd-SA

The structure of the Pd species in ECN-Pd-SA after impregnation is of high interest as it is the starting point for all transformations under reaction conditions. In this chapter, we summarize and discuss the information that leads to the identification of a coordination environment for Pd.

XPS investigations clearly show the presence of Pd species with different electron densities (Fig. 1 e). At least two distinct species are present. The measured binding energies indicate the presence of Pd^{2+} species. Furthermore, XAS and STEM exclude the presence of significant amounts of Pd clusters or nanoparticles in ECN-Pd-SA (Fig. 1 a,b,f). We therefore assume that the presence of Pd species with different electron densities is caused by Pd coordinated in distinctly different configurations and not by differences in formal

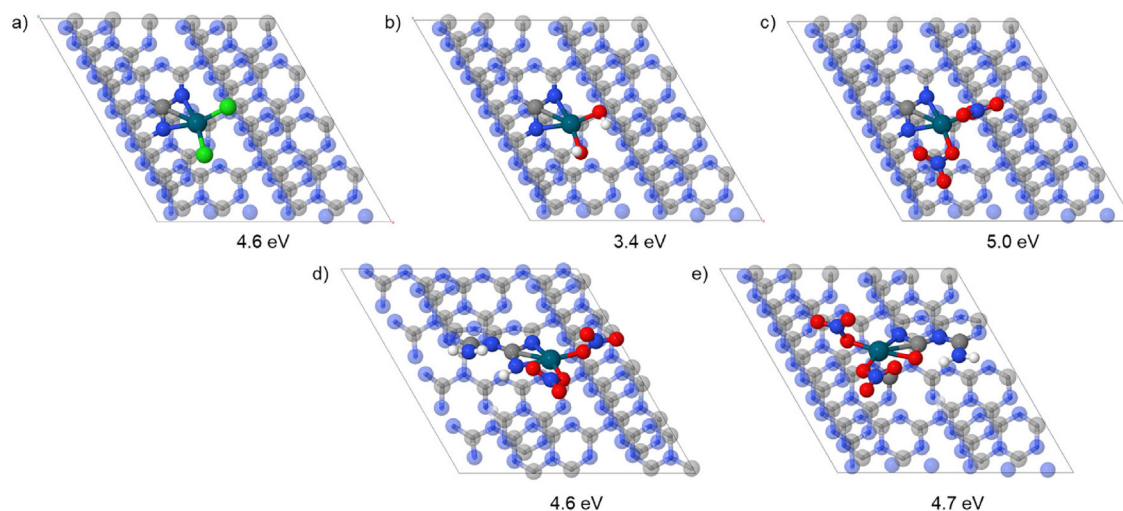


Fig. 7. Top view of DFT-optimized structures of palladium coordinated to two pyridinic nitrogen and two Cl^- (a), OH^- (b) or NO_3^- (c) as well as coordinated to two NO_3^- , one pyridinic nitrogen and one imine group (d) or one carbonyl group (e). Calculated core-level binding energies relative to a surface Pd on a Pd(111) slab are given under the respective structure. Color code: blue: nitrogen, gray: carbon, red: oxygen, green: chlorine, white: hydrogen, teal: palladium. (For interpretation of the references to color in this figure legend, the reader is referred to the web version of this article.)

oxidation state. If K_2PdCl_4 is used as a precursor instead of $\text{Pd}(\text{NH}_3)_4(\text{NO}_3)_2$, a quasi-identical XPS spectrum is obtained, albeit with a shift of 0.4 eV to lower binding energies (Fig. S 18). This indicates that the observed splitting in different coordination environments most likely arises from the support structure. A similar observation has been made for Pt coordinated to a structurally similar covalent triazine framework [51].

Calculating Pd core-level binding energies reveals a difference of 0.4 eV between coordination to two pyridinic nitrogen sites and one pyridinic nitrogen and one imine nitrogen. This is less than the difference observed experimentally for the two identified species (1.7 eV, (Fig. 1 e)) but underlines, that differences in coordination geometry that arise from functional groups on the support have the potential to cause the observed shifts in Pd binding energy.

Due to heterogeneity of the support caused by a multitude of functional groups, it is not possible to assign one structure to Pd after impregnation. Nevertheless, some statements about the chemical environment of Pd can be made. EXAFS fits support the assumption that Pd is coordinated to four ligands (Table S 2). For a palladium in oxidation state 2, which is suggested by XPS and XAS measurements, two L and two X^- ligands would have to be present. XAS results do not allow differentiating between the two types of ligands. Accordingly, both types of ligands are N or O species. Calculation of core level binding energies and comparison to ECN impregnated with K_2PdCl_4 suggest that NO_3^- groups are the X ligands. Non-uniformity of coordination environment is caused by different functional groups on the support. However, DFT calculations suggest that coordinating to N species is energetically more favorable than to O species. Therefore, a formula of $\text{Pd}(\text{N}_{\text{ECN}})_2(-\text{NO}_3)_2$ can be assigned to the Pd single-atoms coordinated to the graphitic carbon nitride.

4.2. Nature of the active species

The nature of the active site is a hotly disputed topic in the area of supposedly single-atom catalysis. We observed that catalytic activity in ethylene hydrogenation as well as in the H_2 - D_2 exchange reaction of Pd in g-CN is accompanied by formation of palladium clusters/nanoparticles. That leads to the conclusion that

these clusters/nanoparticles and not single-atoms are the active species in hydrogenation. This is in agreement with the results of Liu *et al.* [52], Rossell *et al.* [53] and Perez-Aguilar *et al.* [54] who found that in oxidic support small clusters are the active species in hydrogenation reactions and H_2 - D_2 exchange. They are also in agreement with the results of Gates' group, which found that Ir clusters and Rh pairs on MgO significantly increase catalytic activity in ethylene hydrogenation compared to single atoms.[5,7] However, this conclusion contrasts with the findings of Perez Ramirez's group, who used metal single-atoms on g-CN for alkyne hydrogenations. On the other hand, this group has also demonstrated that ensembles of multiple palladium atoms significantly increase reactivity in alkyne hydrogenation [26].

Taking into account the difficulties in distinguishing between single-atoms and clusters that are also described in this work, we do not consider it impossible that small amounts of Pd clusters which nevertheless dominate the catalytic activity also exist in other literature systems. An impressive example from our study is the significantly higher activity in the H_2 - D_2 exchange reaction after activation in ethylene hydrogenation with simultaneously minimal changes in XPS and XAS. There is a risk that these minimal changes will be dismissed as insignificant or within the margin of error. In fact, these changes gained significance in this work only as data points in a trend, underscoring the power of material analysis at several points in the course of the reaction.

The activation of hydrogen is a crucial intermediate step in any kind of hydrogenation reaction. The lack of activity of ECN-Pd-SA in H_2 - D_2 exchange therefore casts doubt on the activity of palladium single-atoms on g-CN in hydrogenation reactions in general. However, we cannot rule out the possibility that hydrogenation of some species (e.g. alkynes) is mechanistically different to alkenes and the H_2 - D_2 exchange in such a way that it enables hydrogenation catalysis by single-atoms. Further research should focus on *in-operando* XAS studies (in order to prevent falsification of results through contact with air as it was observed by Liu *et al.* [52]) of the same catalytic system in hydrogenation of alkenes as well as alkynes. This approach can answer the question of whether the activity of single atoms in hydrogenation catalysis depends on the reactant.

4.3. Agglomeration

Agglomeration to clusters and therefore activation of the metal for the catalytic reactions only takes place in presence of both hydrogen and ethylene. This raises the question about the role of each gas in the agglomeration process.

The formation of metal hydrides is considered to play a crucial role in the destabilization of metal single-atoms on oxide supports [6]. The significant decrease of the main peak at 1.48 Å in the EXAFS for ECN-Pd-SA-100 °C (Fig. 5 b) could be an indication for the formation of palladium hydride. However, for the nitrogen-containing support studied here, the presence of ethylene is also required for agglomeration. This is in contrast to oxide supports where ethylene induces dispersion of metal species [55,56]. Indeed, no decrease in activity is observed in an ethylene atmosphere, which generally argues against a dispersive function of this gas for the system studied here. This underlines that the carrier plays a crucial role in determining the metal dynamics.

We speculate that substitution of ethylene for the nitrogen ligands from the support is required to achieve sufficiently high mobility. Unfortunately, IR studies that would allow identifying such intermediate species are very challenging with amorphous carbon–nitrogen polymers. XAS is not able to differentiate between O and N ligands and has further difficulty in detecting the low concentrated intermediate species. Combining XAS with X-ray emission spectroscopy might allow differentiating individual ligands in the future [57,58]. Together with ever decreasing requirements for metal concentration in modern beamlines, this opens interesting avenues for investigating single-atom dynamics.

Apart from activating the material for catalytic hydrogenation and H₂-D₂ exchange, ethylene also plays a crucial role in retaining the activity. Whether no deactivation is observed in ethylene hydrogenation, fast deactivation is observed in H₂-D₂ exchange after prior activation in ethylene hydrogenation. This deactivation is probably associated with a loss in Pd surface area. This indicates that once formed clusters further agglomerate in an atmosphere that only contains hydrogen. Thus, the stabilizing effect of ethylene on catalytic performance could be caused in two ways: (1) ethylene induces redispersion of larger Pd aggregates and therefore establishes particle size equilibrium (2) ethylene and hydrogen constantly form new clusters by mobilizing single-atoms and therefore compensating for the surface loss that results from the formation of larger aggregates from these clusters.

On another note, the results presented herein show the influence of support on the stability of metal single-atoms. While agglomeration of Pt on SAPO-37 is already observed at 30 °C and of Ir on zeolite HY already at room temperature, it requires a temperature of 100 °C for agglomeration of Pd on g-CN. Single-atoms therefore undergo higher stabilization on nitrogen containing carbons than on oxides. This is consistent with recent results from our group demonstrating the stability of Ir single atoms on a covalent triazine framework (a related C-N material) in a hydrogen stream up to 400 °C [59].

5. Conclusion

By using AC-STEM, XPS and XAS over the course of the reaction, it was shown that a single-atom palladium catalyst agglomerates during ethylene hydrogenation at 100 °C. This agglomeration coincides with the appearance of catalytic activity, suggesting that small clusters, rather than single atoms, are the active species. The agglomeration process requires both ethylene and hydrogen and is a necessary prerequisite for hydrogen activation, as was demonstrated by H₂-D₂ exchange experiments. This raises general

questions regarding the activity of palladium single-atoms on g-CN in hydrogenation reactions.

The results show the usefulness of studying the metal dynamics over the course of reaction in order to identify the active species. Understanding this dynamic behavior, and in particular the influence of gas atmosphere and temperature, opens up new ways to influence metal speciation and thus the possibility of a more rational design of catalysts.

Data availability

Data will be made available on request.

Declaration of Competing Interest

The authors declare that they have no known competing financial interests or personal relationships that could have appeared to influence the work reported in this paper.

Acknowledgments

The authors thank Diamond Light Source for providing beamtime on beamline I20-EDE (SP29667-1). Daniel Ditz and Chalachew Mebrahtu are thanked for fruitful discussion on the subject.

This work was performed as part of the Cluster of Excellence Fuel Science Center (EXC 2186, ID: 390919832) funded by the Excellence Initiative by the German federal and state governments to promote science and research at German universities. M.V. thanks Konrad-Adenauer-Stiftung for funding. A.I. acknowledges funding of the German Academic Scholarship Foundation. N.M.S. thanks RWTH Aachen University for financial support. M.H. and A.M. acknowledge financial support by the Deutsche Forschungsgemeinschaft (DFG) in the project HE 7192/7-1.

We acknowledge the support of Hitachi High-Technologie.

Appendix A. Supplementary material

Supplementary data to this article can be found online at <https://doi.org/10.1016/j.jcat.2023.03.011>.

References

- [1] L. Liu, A. Corma, *Chem. Rev.* 118 (2018) 4981–5079.
- [2] B.C. Gates, *Trends Chem.* 1 (2019) 99–110.
- [3] A. Beniya, S. Higashi, *Nat. Catal.* 2 (2019) 590–602.
- [4] S.K. Kaiser, Z. Chen, D. Faust Akl, S. Mitchell, J. Pérez-Ramírez, *Chem. Rev.* 120 (2020) 11703–11809.
- [5] J. Lu, P. Serna, C. Aydin, N.D. Browning, B.C. Gates, *J. Am. Chem. Soc.* 133 (2011) 16186–16195.
- [6] J. Lu, C. Aydin, N.D. Browning, B.C. Gates, *J. Am. Chem. Soc.* 134 (2012) 5022–5025.
- [7] E. Guan, B.C. Gates, *ACS Catal.* 8 (2018) 482–487.
- [8] Z. Jakub, J. Hulva, M. Meier, R. Bliem, F. Kraushofer, M. Setvin, M. Schmid, U. Diebold, C. Franchini, G.S. Parkinson, *Angew. Chemie* 131 (2019) 14099–14106.
- [9] L. DeRita, J. Resasco, S. Dai, A. Boubnov, H.V. Thang, A.S. Hoffman, I. Ro, G.W. Graham, S.R. Bare, G. Pacchioni, et al., *Nat. Mater.* 18 (2019) 746–751.
- [10] L. Liu, D.N. Zakharov, R. Arenal, P. Concepcion, E.A. Stach, A. Corma, *Nat. Commun.* 9 (2018) 574.
- [11] S.K. Kaiser, E. Fako, I. Surin, F. Krumeich, V.A. Kondratenko, E.V. Kondratenko, A.H. Clark, N. López, J. Pérez-Ramírez, *Nat. Nanotechnol.* 17 (2022) 606–612.
- [12] M.B. Gawande, P. Fornasiero, R. Zbořil, *ACS Catal.* 10 (2020) 2231–2259.
- [13] C. Rivera-Cárcamo, P. Serp, *ChemCatChem* 10 (2018) 5058–5091.
- [14] G. Gao, Y. Jiao, E.R. Waclawik, A. Du, *J. Am. Chem. Soc.* 138 (2016) 6292–6297.
- [15] X. Li, P. Cui, W. Zhong, J. Li, X. Wang, Z. Wang, J. Jiang, *Chem. Commun.* 52 (2016) 13233–13236.
- [16] Y. Yang, F. Li, J. Chen, J. Fan, Q. Xiang, *ChemSusChem* 13 (2020) 1979–1985.
- [17] T. He, C. Zhang, L. Zhang, A. Du, *Nano Res.* 12 (2019) 1817–1823.
- [18] J. Feng, H. Gao, L. Zheng, Z. Chen, S. Zeng, C. Jiang, H. Dong, L. Liu, S. Zhang, X. Zhang, *Nat. Commun.* 11 (2020) 4341.
- [19] X. Lv, W. Wei, H. Wang, B. Huang, Y. Dai, *Appl. Catal. B Environ.* 264 (2020).
- [20] X. Liu, Y. Deng, L. Zheng, M.R. Kesama, C. Tang, Y. Zhu, *ACS Catal.* 12 (2022) 5517–5526.

- [21] G. Vilé, D. Albani, M. Nachttegaal, Z. Chen, D. Dontsova, M. Antonietti, N. López, J. Pérez-Ramírez, *Angew. Chemie Int. Ed.* 54 (2015) 11265–11269.
- [22] Z. Chen, S. Mitchell, E. Vorobyeva, R.K. Leary, R. Hauert, T. Furnival, Q.M. Ramasse, J.M. Thomas, P.A. Midgley, D. Dontsova, et al., *Adv. Funct. Mater.* 27 (2017) 1605785.
- [23] E. Vorobyeva, Z. Chen, S. Mitchell, R.K. Leary, P. Midgley, J.M. Thomas, R. Hauert, E. Fako, N. López, J. Pérez-Ramírez, *J. Mater. Chem. A* 5 (2017) 16393–16403.
- [24] X. Huang, Y. Xia, Y. Cao, X. Zheng, H. Pan, J. Zhu, C. Ma, H. Wang, J. Li, R. You, et al., *Nano Res.* 10 (2017) 1302–1312.
- [25] Z. Chen, E. Vorobyeva, S. Mitchell, E. Fako, M.A. Ortuño, N. López, S.M. Collins, P.A. Midgley, S. Richard, G. Vilé, et al., *Nat. Nanotechnol.* 13 (2018) 702–707.
- [26] E. Vorobyeva, E. Fako, Z. Chen, S.M. Collins, D. Johnstone, P.A. Midgley, R. Hauert, O.V. Safonova, G. Vilé, N. López, et al., *Angew. Chemie Int. Ed.* 58 (2019) 8724–8729.
- [27] J. Li, S. Zhao, S.Z. Yang, S. Wang, H. Sun, S.P. Jiang, B. Johannessen, S. Liu, J. Mater. Chem. A 9 (2021) 3029–3035.
- [28] J. Büker, X. Huang, J. Bitzer, W. Kleist, M. Muhler, B. Peng, *ACS Catal.* 11 (2021) 7863–7875.
- [29] Z. Chen, E. Vorobyeva, S. Mitchell, E. Fako, N. López, S.M. Collins, R.K. Leary, P.A. Midgley, R. Hauert, J. Pérez-Ramírez, *Natl. Sci. Rev.* 5 (2018) 642–652.
- [30] S. Büchele, A. Yakimov, S.M. Collins, A. Ruiz-Ferrando, Z. Chen, E. Willinger, D. M. Kepaptsoglou, Q.M. Ramasse, C.R. Müller, O.V. Safonova, et al., *Small* (2022) 2202080.
- [31] K. Qi, M. Chhowalla, D. Voiry, *Mater. Today* 40 (2020) 173–192.
- [32] D.J. Morgan, *Surf. Sci. Spectra* 28 (2021).
- [33] S. Diaz-Moreno, M. Amboage, M. Basham, R. Boada, N.E. Bricknell, G. Cibir, T. M. Cobb, J. Filik, A. Freeman, K. Geraki, et al., *J. Synchrotron Radiat.* 25 (2018) 998–1009.
- [34] S. Diaz-Moreno, S. Hayama, M. Amboage, A. Freeman, J. Sutter, G. Duller, *J. Phys. Conf. Ser.* 190 (2009).
- [35] J. Headspith, J. Groves, P. N. Luke, M. Kogimtzis, G. Salvini, S. L. Thomas, R. C. Farrow, J. Evans, T. Rayment, J. S. Lee, et al., in *2007 IEEE Nucl. Sci. Symp. Conf. Rec., IEEE, 2007*, pp. 2421–2428.
- [36] B. Ravel, M. Newville, *Phys. Scr.* T115 (2005) 1007.
- [37] G. Kresse, J. Hafner, *Phys. Rev. B* 49 (1994) 14251–14269.
- [38] G. Kresse, J. Furthmüller, *Comput. Mater. Sci.* 6 (1996) 15–50.
- [39] J.P. Perdew, K. Burke, M. Ernzerhof, *Phys. Rev. Lett.* 77 (1996) 3865–3868.
- [40] S.N. Steinmann, C. Corminboeuf, *J. Chem. Theory Comput.* 7 (2011) 3567–3577.
- [41] P.E. Blöchl, *Phys. Rev. B* 50 (1994) 17953–17979.
- [42] G. Kresse, D. Joubert, *Phys. Rev. B* 59 (1999) 1758–1775.
- [43] H.J. Monkhorst, J.D. Pack, *Phys. Rev. B* 13 (1976) 5188–5192.
- [44] K.K. Irikura, D.J. Furip, *Computational Thermochemistry*, American Chemical Society, 1998.
- [45] K.S. Kim, A.F. Gossman, N. Winograd, *Anal. Chem.* 46 (1974) 197–200.
- [46] M.C. Militello, S.J. Simko, *Surf. Sci. Spectra* 3 (1994) 402–409.
- [47] W.P. Zhou, A. Lewera, R. Larsen, R.I. Masel, P.S. Bagus, A. Wieckowski, *J. Phys. Chem. B* 110 (2006) 13393–13398.
- [48] J.E. Park, S.G. Park, A. Koukitu, O. Hatozaki, N. Oyama, *Synth. Met.* 141 (2004) 265–269.
- [49] D. Ketenoglu, *X-Ray Spectrom.* (2022) 1–22.
- [50] S. Krüger, S. Vent, F. Nörtemann, M. Staufer, N. Rösch, *J. Chem. Phys.* 115 (2001) 2082–2087.
- [51] M. Soorholtz, L.C. Jones, D. Samuelis, C. Weidenthaler, R.J. White, M.M. Titirici, D.A. Cullen, T. Zimmermann, M. Antonietti, J. Maier, et al., *ACS Catal.* 6 (2016) 2332–2340.
- [52] L. Liu, D.M. Meira, R. Arenal, P. Concepcion, A.V. Puga, A. Corma, *ACS Catal.* 9 (2019) 10626–10639.
- [53] M.D. Rossell, F.J. Caparrós, I. Angurell, G. Muller, J. Llorca, M. Seco, O. Rossell, *Catal. Sci. Technol.* 6 (2016) 4081–4085.
- [54] J.E. Perez-Aguilar, J.T. Hughes, C.-Y. Chen, B.C. Gates, *Catal. Sci. Technol.* 11 (2021) 6666–6681.
- [55] A. Uzun, B.C. Gates, *Angew. Chemie - Int. Ed.* 47 (2008) 9245–9248.
- [56] A. Uzun, B.C. Gates, *J. Am. Chem. Soc.* 131 (2009) 15887–15894.
- [57] G. Smolentsev, A.V. Soldatov, J. Messinger, K. Merz, T. Weyhermüller, U. Bergmann, Y. Pushkar, J. Yano, V.K. Yachandra, P. Glatzel, *J. Am. Chem. Soc.* 131 (2009) 13161–13167.
- [58] J.C. Swarbrick, Y. Kvashnin, K. Schulte, K. Seenivasan, C. Lamberti, P. Glatzel, *Inorg. Chem.* 49 (2010) 8323–8332.
- [59] A. Iemhoff, M. Vennewald, J. Artz, C. Mebrahtu, A. Meledin, T.E. Weirich, H. Hartmann, A. Besmehn, M. Aramini, F. Venturini, et al., *ChemCatChem* 14 (2022) e20220019.